Optical solitons and optical patterns controlled by a moiré lattice potential in a Rydberg atomic gas

Zeyun Shi,[1] Lu Qin,[2] Yuan Zhou,[1] Yu Zhong,[1] Guanghui Wang,[3] and Haibo Huang[1]

[1]*School of Electrical and Information Engineering, Hubei Key Laboratory of Energy Storage and Power Battery, Shiyan Key Laboratory of Electromagnetic Induction and Energy Saving Technology, Shiyan Key Laboratory of Quantum Information and Precision Optics, Hubei University of Automotive Technology, Shiyan 442002, China*

[2]*Department of Physics, Henan Normal University, Xinxiang 453007, China*

[3]*School of Automobile Engineering, Hubei University of Automotive Technology, Shiyan 442002, China*

(Received 26 May 2024; accepted 29 July 2024; published 12 August 2024)

We investigate the optical soliton and patterns within a system exhibiting a ladder-type Rydberg electromagnetically induced transparency configuration, controlled by a moiré lattice potential. By designing theoretically the optical moiré lattice, we study its localization-delocalization transition and numerically demonstrate the conditions for stable high-dimensional solitons in a commensurate and an incommensurate moiré lattice, respectively. Through modulation instability analysis and numerical simulations, on the one hand, we find that the solitons and vortices exhibit exceptional stability in the self-focusing Kerr nonlinear system. On the other hand, our simulations further reveal the emergence of various extended structures, including polygonal, hexagonal, square, annular, and droplet patterns in self-defocusing Kerr nonlinear system. We also demonstrate various structural phase transitions of the optical patterns by actively manipulating the moiré lattice constant and the strength of nonlinear interactions, resulting in a diverse range of ground-state patterns. Our paper provides a versatile platform for manipulating and controlling light-matter interactions in Rydberg atomic ensembles, opening avenues for future research in designing and controlling complex light structures using Rydberg atomic systems.

DOI: 10.1103/PhysRevA.110.023513

I. INTRODUCTION

Rydberg electromagnetically induced transparency (EIT) has emerged as a fascinating area of research in quantum optics, combining the phenomenon of EIT with the strong, long-range interactions between highly excited Rydberg atoms [1–7]. This combination allows for precise manipulation of optical properties in atomic gases, paving the way for various applications in fields such as nonlinear optics, quantum information processing, quantum storage, quantum many-body simulation, precision measurement and sensing, and quantum metrology [2–13].

In EIT, the control and the probe laser fields interact with a three-level atomic system, resulting in quantum interference that allows for the transparent propagation of the probe laser under certain conditions [1]. In the presence of Rydberg interactions, which can be attractive or repulsive depending on the states involved, this transparency can be influenced by the interaction between Rydberg atoms [2,14]. This leads to nonlinear optical effects that can modify the propagation of light in complex ways [7,15,16].

The use of moiré optical lattices [17–21] in combination with Rydberg EIT opens new avenues for exploring the interplay between periodic potential structures and nonlinear optical effects. Moiré lattices arise from the superposition of two periodic lattices with different rotation angles, leading to a variety of lattice patterns and symmetries. The modulation of light in such lattices can lead to unique behaviors such as localization-delocalization transitions (LDTs) [20,21], insulating states [22], unconventional superconductivity [23], quantum Hall effect [24], slow light, nonlinear effects, chiral plasma, superfluid to Mott insulator phase transition of Bose-Einstein condensate, and light solitons [19,21,25–32].

Symmetry breaking and formation of localized structures (solitons) or extended ordered structures (patterns) via some instability mechanisms are very interesting and important phenomena [33–35]. One of the crucial aspects of this field is the study of modulation instability (MI), a phenomenon characterized by the exponential growth of perturbations on a continuous wave due to nonlinear modulational interaction of the plane wave [36–40]. In Rydberg systems, MI can manifest as long-wavelength or short-wavelength instability, depending on whether the underlying nonlinearity is self-focusing or self-defocusing [15,41–43]. With the onset of the MI, various self-organized patterns were found in Rydberg-dressed atomic gases [44–51]. However, investigation of spontaneous pattern formation under moiré potential in the Rydberg atomic gases is still lacking. This motivated us to study the novel pattern formation in such a system.

In this paper, we propose a scheme to investigate the nonlocal high-dimensional optical solitons and stationary optical pattern formations in a cold ladder-type Rydberg-EIT configuration subjected to a moiré lattice potential. We first design theoretically an electromagnetically induced moiré lattice and investigate in detail localization-delocalization transition. Based on MI analysis and numerical simulations, we numerically demonstrate the condition for the stable soliton in commensurate and incommensurate moiré lattices. We further observe that Hermite-Gaussian (HG) solitons, Laguerre-Gaussian (LG) solitons, and vortices show

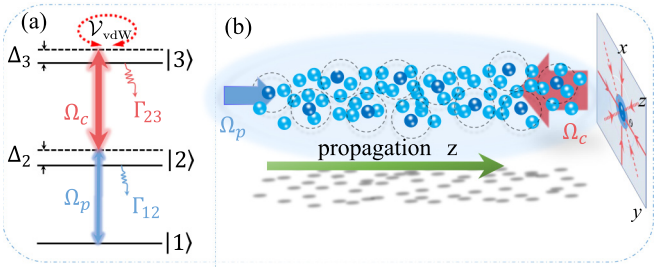

FIG. 1. (a) Level diagram and excitation scheme of the Rydberg EIT. Weak probe (blue) and strong control (red) laser fields with central angular frequencies ω_p and ω_c as well as half-Rabi frequencies Ω_p and Ω_c drive the transitions $|1\rangle \leftrightarrow |2\rangle$ and $|2\rangle \leftrightarrow |3\rangle$, respectively. The Rydberg atoms interact with each other according to the van der Waals potential $\hbar\mathcal{V}_{\rm vdW}(\mathbf{r}'-\mathbf{r}) \equiv -\hbar C_6/|\mathbf{r}'-\mathbf{r}|^6$. Δ_2 and Δ_3 are respectively the one- and two-photon detunings. $\Gamma_{\alpha\beta}$ is the spontaneous emission decay rate from the $|\beta\rangle$ to $|\alpha\rangle$ ($\alpha = 1, 2; \beta = 3$). (b) Possible experimental geometry, where small solid circles denote atoms and large dashed circles denote Rydberg blockade spheres. Inset: The control field consisting of two groups of orthogonalized paired standing waves paraxially propagating along the $-z$ axis, twisted by a small angle θ.

remarkable stability for self-focusing Kerr nonlinearity. Our simulations also reveal the formation of various extended structures such as polygonal, hexagonal, square, annular, and droplet patterns under self-defocusing Kerr nonlinearity. Furthermore, we witness different structural phase transitions in optical patterns when adjusting the moiré lattice constant and the strength of nonlinear interaction, leading to a variety of ground-state patterns. Our paper provides a versatile platform for manipulating and controlling light-matter interactions in Rydberg atomic ensembles, and emphasizes the potential for exploring novel optical phenomena and solitonic behavior in systems with strong nonlocal nonlinearities.

The remainder of the paper is arranged as follows. In Sec. II, we present the physical model of the Rydberg EIT under study and derive a three-dimensional [(2 + 1)D] nonlocal nonlinear Schrödinger (NNLS) equation describing the evolution of the probe field beyond mean-field approximation. In Sec. III, we design theoretically an electromagnetically induced moiré lattice and investigate localization-delocalization transition. In Sec. IV, we respectively consider the MI of a plane-wave state, explore the condition for the stable soliton in commensurate and incommensurate moiré lattices, and investigate the nonlocal optical soliton and vortices. In Sec. V, we present various optical pattern formations and their structural phase transition in the system. Finally, Sec. VI gives a summary of the main results obtained in our paper.

II. PHYSICAL MODEL

We consider an ensemble of lifetime-broadened three-level atomic gas exhibiting a ladder-type level configuration, depicted schematically in Fig. 1(a). In this setup, a weak probe laser field, characterized by its central angular frequency ω_p and wave vector $\mathbf{k}_p$, drives the transition $|1\rangle \leftrightarrow |2\rangle$. Concurrently, a strong control laser field with central angular frequency ω_c and wave vector $\mathbf{k}_c$ stimulates the transitions $|2\rangle \leftrightarrow |3\rangle$. Therefore, the total electric fields acting within the atomic ensemble can be expressed as $\mathbf{E}(\mathbf{r}, t) = \mathbf{e}_p\mathcal{E}_p \exp\{i(\mathbf{k}_p \cdot \mathbf{r} - \omega_p t)\} + \mathbf{E}_c(\mathbf{r}, t) + \text{H.c.}$, with $\mathbf{e}_p$ and $\mathcal{E}_p$ the unit vector of the polarization direction and the envelope of the probe field, respectively. For the control field, we consider two sets of orthogonalized paired standing waves propagating paraxially along the $-z$ axis, each twisted by a small angle θ, as illustrated in the inset of Fig. 1(b). Consequently, the entire control field can be represented in the form $\mathbf{E}_c(\mathbf{r}, t) = \sum_{j=1}^{4} \mathbf{E}_{cj}(\mathbf{r}, t)$, where $\mathbf{E}_{c1} = E_1 \cos(k_0 x)[e^{i\phi}\hat{x} + e^{i(\phi-\pi/2)}\hat{y}]$, $\mathbf{E}_{c2} = E_1 \cos(k_0 y)[e^{i(\phi+\pi/2)}\hat{x} + e^{i\phi}\hat{y}]$, $\mathbf{E}_{c3} = E_2 \cos(k_0 x')[e^{i\phi}\hat{x}' + e^{i(\phi-\pi/2)}\hat{y}']$, and $\mathbf{E}_{c4} = E_2 \cos(k_0 y')[e^{i\phi}\hat{x}' + e^{i(\phi-\pi/2)}\hat{y}']$, with $k_0 = k_c \sin(\theta)$, E_1 and E_2 representing the amplitude of the two groups of standing waves, $\phi = k_c \cos(\theta) z - \omega_c t$, $\hat{x}$ and $\hat{y}$ being the unit vectors along the x and y axis, and $\hat{x}'$ and $\hat{y}'$ being the unit vector related to $\hat{x}$ and $\hat{y}$ via the two-dimensional (2D) rotation by angle θ. Therefore, by varying the twisted angle θ and amplitude ratio E_2/E_1, the interference of control fields will produce different spatial distributions and induce an effective 2D moiré lattice in the xy plane.

The ground state $|1\rangle$, the ordinary excited state $|2\rangle$, and the highly excited Rydberg state $|3\rangle$ consist of the Rydberg EIT. With the electric dipole and rotating-wave approximations, and incorporating the atom-atom interactions, the Hamiltonian of the system in the interaction picture is expressed as

$$\mathcal{H}_I = \sum_{\alpha=2}^{3} \Delta_\alpha \hat{S}_{\alpha\alpha}(\mathbf{r}, t) - \hbar(\Omega_p \hat{S}_{12} + \Omega_c \hat{S}_{23} + \text{H.c.}) + \frac{1}{2}\mathcal{N}_a \int d^3\mathbf{r}' \hat{S}_{33}(\mathbf{r}, t)\hbar\mathcal{V}_{\rm vdW}(\mathbf{r}' - \mathbf{r})\hat{S}_{33}(\mathbf{r}', t), \quad (1)$$

where $\mathcal{N}_a$ denotes the atomic density. The half Rabi frequencies of the probe and control fields are denoted as $\Omega_p = \mathbf{e}_p \cdot \mathbf{p}_{21}\mathcal{E}_p/\hbar$ and $\Omega_c = \mathbf{e}_c \cdot \mathbf{p}_{32}\mathcal{E}_c/\hbar$, respectively. Here $\mathbf{p}_{\alpha\beta}$ represents the electric dipole matrix element associated with the transition from $|\beta\rangle$ to $|\alpha\rangle$. The transition operator $\hat{S}_{\alpha\beta} = |\beta\rangle\langle\alpha| \exp\{i[(\mathbf{k}_\beta - \mathbf{k}_\alpha) \cdot \mathbf{r} - (\omega_\beta - \omega_\alpha + \Delta_\beta - \Delta_\alpha)t]\}$ satisfies the commutation relation $[\hat{S}_{\alpha\beta}(\mathbf{r}, t), \hat{S}_{\alpha'\beta'}(\mathbf{r}', t)] = \mathcal{N}_a^{-1}\delta(\mathbf{r} - \mathbf{r}')[\delta_{\alpha\beta'}\hat{S}_{\alpha'\beta}(\mathbf{r}, t) - \delta_{\alpha'\beta}\hat{S}_{\alpha\beta'}(\mathbf{r}', t)]$, with the one- and two-detunings given by $\Delta_2 = \omega_p - (\omega_2 - \omega_1)$ and $\Delta_3 = \omega_c + \omega_p - (\omega_3 - \omega_1)$, respectively. The last term on the right-hand side of Eq. (1) is the contribution of the Rydberg-Rydberg interaction with $\hbar\mathcal{V}_{\rm vdW}(\mathbf{r}' - \mathbf{r}) \equiv -\hbar C_6/|\mathbf{r}' - \mathbf{r}|^6$ the long-range interaction potential (i.e., the interaction at position $\mathbf{r}$ is influenced by the vicinity position $\mathbf{r}'$) and C_6 the dispersive parameter.

According to the Hamiltonian given by Eq. (1), the dynamics of atoms in the system is governed by the optical Bloch equation, given by

$$\frac{\partial\rho}{\partial t} = -\frac{i}{\hbar}[\mathcal{H}_I, \rho] - \Gamma[\rho], \quad (2)$$

where ρ is a 3×3 density matrix (DM, with density-matrix elements $\rho_{\alpha\beta}$; $\alpha, \beta = 1, 2, 3$) describing the atomic population and coherence, and Γ is a 3×3 relaxation matrix describing the spontaneous emission and dephasing. Explicit expressions of $\rho_{\alpha\beta}(\mathbf{r}, t)$ are presented in the Appendix.

Additionally, under the condition of slow-varying envelope approximation, the probe field described by the Maxwell equation takes the form

$$i\left(\frac{\partial}{\partial z}+\frac{1}{c}\frac{\partial}{\partial t}\right)\Omega_p+\frac{c}{2\omega_p}\nabla_\perp^2\Omega_p+\frac{\omega_p}{2c}\chi_p\Omega_p=0, \quad (3)$$

where $\nabla_\perp^2=\frac{\partial^2}{\partial x^2}+\frac{\partial^2}{\partial y^2}$, $\chi_p=\mathcal{N}_a(\mathbf{e}_p\cdot\mathbf{p}_{12})^2\rho_{21}/(\varepsilon_0\hbar\Omega_p)$ is the probe-field susceptibility with c and ε_0 the vacuum speed of the light and dielectric coefficient of vacuum, respectively. Without loss of generality, we assume the probe field propagates along the z direction, i.e., $\mathbf{k}_p=(0,0,\omega_p/c)$. Meanwhile, we orient the strong control laser field along with $\mathbf{k}_c=(0,0,-k_c)$ to minimize the first-order Doppler effect. Additionally, since we consider a stationary state of the system, the time derivatives in the Maxwell-Bloch equations (2) and (3) can be neglected (i.e., $\partial/\partial t=0$). This assumption holds valid if the probe and control fields have sufficiently long durations, i.e., they are continuous-wave fields.

Since the probe field is weaker than the control field, the standard asymptotic perturbation expansion [52] can be applied to solve the Bloch equation (2) by considering Ω_p as a small parameter. The solution of Eq. (2) up to third order is provided in the Appendix. Using this solution, we derive the expression for the total optical susceptibility of the probe field:

$$\chi_p=\chi_p^{(1)}+\chi_{p,\mathrm{loc}}^{(3)}|\Omega_p|^2+\int d^3\mathbf{r}'\chi_{p,\mathrm{nloc}}^{(3)}(\mathbf{r}'-\mathbf{r})|\Omega_p(\mathbf{r}')|^2, \quad (4)$$

where $\chi_p^{(1)}=\mathcal{N}_a|\mathbf{e}_p\cdot\mathbf{p}_{12}|^2a_{21}^{(1)}/(\varepsilon_0\hbar)$ is the linear susceptibility, $\chi_{p,\mathrm{loc}}^{(3)}=\mathcal{N}_a|\mathbf{e}_p\cdot\mathbf{p}_{12}|^2a_{21,1}^{(3)}/(\varepsilon_0\hbar)$ is the third-order nonlinear susceptibility contributed from local interaction between atoms, and $\chi_{p,\mathrm{nloc}}^{(3)}=\mathcal{N}_a^2|\mathbf{e}_p\cdot\mathbf{p}_{12}|^2a_{21,2}^{(3)}a_{33,31}^{(3)}(\mathbf{r}'-\mathbf{r})\mathcal{V}_{\mathrm{vdW}}(\mathbf{r}'-\mathbf{r})/(\varepsilon_0\hbar)$ is a nonlocal nonlinear susceptibility appearing in Rydberg EIT. Explicit expressions of $a_{21}^{(1)}$, $a_{21,1}^{(3)}$, $a_{21,2}^{(3)}$, and $a_{33,31}^{(3)}(\mathbf{r}'-\mathbf{r})$ are, respectively, given in the Appendix [see Eqs. (A2), (A7), and (A12)]. We see from the above expression that the nonlocal third-order nonlinear susceptibility $\chi_{p,\mathrm{nloc}}^{(3)}(\mathbf{r})$ is space dependent.

A local approximation along the z direction can be made under the condition of which the spatial length of the probe pulse in the z direction is much larger than the range of atom-atom interactions. Consequently, the last term on the right side of Eq. (4) can be reduced as $\int d^3r'\chi_{p,\mathrm{nloc}}^{(3)}(\mathbf{r}'-\mathbf{r})|\Omega_p(\mathbf{r}')|^2\approx\iint dr'_\perp\tilde{\chi}_{p,\mathrm{nloc}}^{(3)}(\mathbf{r}'_\perp-\mathbf{r}_\perp)|\Omega_p(\mathbf{r}'_\perp,z)|^2$ with $\tilde{\chi}_{p,\mathrm{nloc}}^{(3)}(\mathbf{r}'_\perp-\mathbf{r}_\perp,z)=\int dz'\chi_{p,\mathrm{nloc}}^{(3)}(\mathbf{r}'-\mathbf{r})$. Finally, we obtain

$$i\frac{\partial\Omega_p}{\partial z}+\frac{c}{2\omega_p}\nabla_\perp^2\Omega_p+\frac{\omega_p}{2c}\chi_p^{(1)}\Omega_p+\frac{\omega_p}{2c}\left[\chi_{p,\mathrm{loc}}^{(3)}|\Omega_p|^2+\iint\mathbf{r}'_\perp\tilde{\chi}_{p,\mathrm{nloc}}^{(3)}(\mathbf{r}'_\perp-\mathbf{r}_\perp)|\Omega_p(\mathbf{r}'_\perp,z)|^2\right]\Omega_p=0, \quad (5)$$

where $\mathbf{r}_\perp=(x,y)$ and $\mathbf{r}'_\perp=(x',y')$.

Taking cold ^{88}Sr as the atomic gas as an example, we assign atomic levels as $|1\rangle=|5s^2\,{}^1S_0\rangle$, $|2\rangle=|5s5p\,{}^1P_1\rangle$, and $|3\rangle=|5sns\,{}^1S_0\rangle$ with n the principal quantum number. For $n=60$, $C_6=-81.6\times2\pi$ GHz μm^6 [53–55]. Typical system parameters are chosen as follows: $\Delta_2=3.87\times10^8\,\mathrm{s}^{-1}$, $\Delta_3=1.53\times10^6\,s^{-1}$, $\Gamma_{21}=0.1\times2\pi$ MHz, $\Gamma_3=6.1\times2\pi$ MHz, $\Omega_c=2.0\times10^7\,\mathrm{s}^{-1}$, and the atomic density $\mathcal{N}_a=1\times10^{11}\,\mathrm{cm}^{-3}$. With these parameters, we calculate and then get $\chi_{p,\mathrm{loc}}^{(3)}\approx(2.1+0.01i)\times10^{-17}\,\mathrm{Hz}^{-2}$, and the maximal value of $\tilde{\chi}_{p,\mathrm{nloc}}^{(3)}\approx(1.1+0.1i)\times10^{-13}\,\mathrm{Hz}^{-2}$.

It is noteworthy that there exists not only the local Kerr nonlinearity contributed by the light-atom interaction but also the nonlocal Kerr nonlinearity resulting from the atom-atom interaction. However, the latter interaction dominates and is orders of magnitude larger than the local one [52]. Eventually, we obtain the NNLS equation of the probe field envelope in dimensionless form:

$$i\frac{\partial u}{\partial s}=-\nabla_\perp^2u+V_{\mathrm{op}}(\vec{\zeta})u+\iint d^2\zeta'\tilde{\Re}(\vec{\zeta}'-\vec{\zeta})|u(\vec{\zeta}',s)|^2u, \quad (6)$$

where $u=\Omega_p/U_0$ is the dimensionless Rabi frequency with U_0 the typical Rabi frequency of the weak probe field. $s=z/(2L_{\mathrm{diff}})$ is defined with $L_{\mathrm{diff}}=\omega_pR_\perp^2/c$ the typical diffraction length, $\vec{\zeta}\equiv(\xi,\eta)=(x,y)/R_\perp$, and $[\vec{\zeta}'=(x',y')/R_\perp]$ are dimensionless spatial coordinates with $R_\perp$ the typical radius of the probe beam. The optical potential is given by $V_{\mathrm{op}}=-\omega_p^2R_\perp^2\chi_p^{(1)}/c^2=\omega_p^2R_\perp^2\mathcal{N}_a|p_{13}|^2\Omega_c/[c^2\varepsilon_0\hbar(|\Omega_c|^2-d_{21}d_{31})]$, and $\tilde{\Re}(\vec{\zeta})=L_{\mathrm{diff}}|U_0|^2R_\perp^2\omega_p\tilde{\chi}_{p2}^{(3)}/c\equiv\sigma a_{44,41}^{(3)}(\vec{\zeta}R_\perp)\mathcal{V}_{\mathrm{vdW}}(\vec{\zeta}R_\perp)$ with $\sigma=|\mathbf{e}_p\cdot\mathbf{p}_{13}|^2a_{31,2}^{(3)}R_\perp^4\omega_p^2U_0^2\mathcal{N}_a^2/(\varepsilon_0\hbar c^2)$. Here we omit the local Kerr nonlinearity since it is much smaller than the nonlocal one.

The equation describes the general situation of the probe field propagating in Rydberg atomic gas with optical potential. The left-hand side of the equation represents propagation term, spatial diffraction term, optical potential term, and nonlocal nonlinearity term, respectively. The property of the nonlocal response function can be adjusted by dispersive parameter C_6, where $C_6<0$ corresponds to self-defocusing and $C_6>0$ corresponds to self-focusing nonlinearity.

III. REALIZATION OF ELECTROMAGNETICALLY INDUCED MOIRÉ LATTICES

A. Realization of an electromagnetically induced moiré lattice

Our primary goal is to investigate the optical soliton and optical pattern formations within the system featuring a moiré potential. To achieve this, our initial focus lies in examining the physical realization of various optical moiré potentials. For the convenience of discussion, we adopt the optical potential expressed as

$$V_{\mathrm{op,T}}(\vec{\zeta})=|p_1V(S\vec{\zeta})+p_2V(\vec{\zeta})|^2, \quad (7)$$

which is referred to as the moiré lattice potential. This potential arises from the superposition of two periodic lattices $V(\vec{\zeta})=\cos(a\xi)+\cos(a\eta)$ mutually rotated by angle θ. Unless otherwise stated, we use $a=2$. Here $S(\theta)$ represents the operator of two-dimensional rotation in the (ξ,η) plane with depths p_1 and p_2. For Pythagorean angles $\theta=\arctan[2mn/(m^2-n^2)]$, where m, $n\in\mathbf{N}$ are associated with the Pythagorean triple $(m^2-n^2,2mn,m^2+n^2)$, the moiré

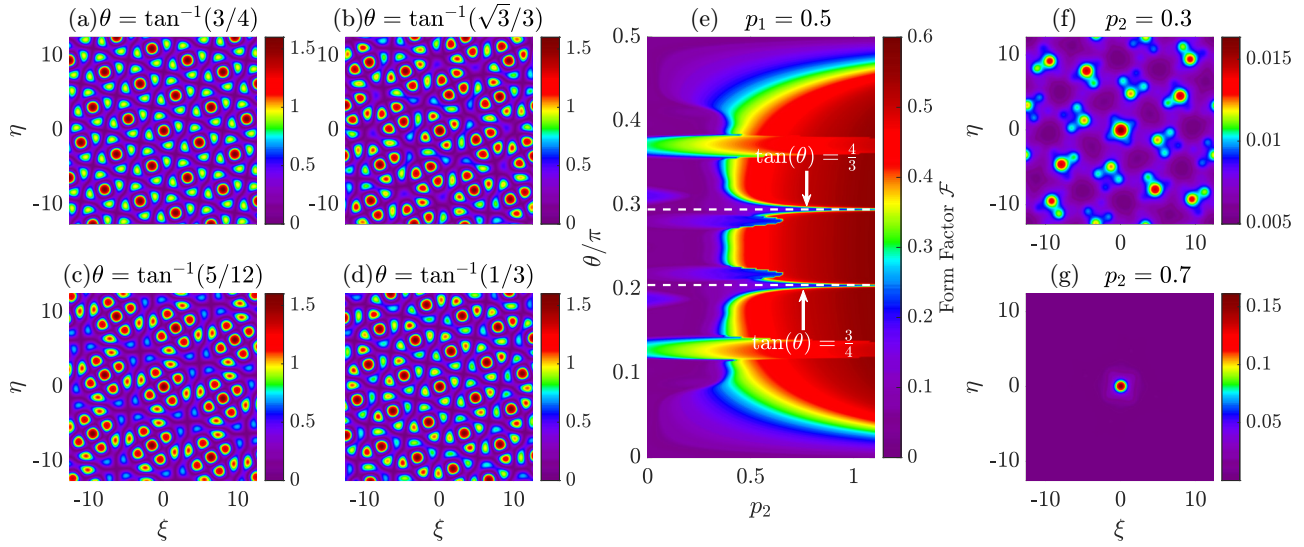

FIG. 2. Various moiré lattices with $p_1 = 0.5$ and $p_2 = 0.3$ for different twisted angles θ: (a) $\theta = \arctan(3/4)$, (b) $\theta = \arctan(\sqrt{3}/3)$, (c) $\theta = \arctan(5/12)$, and (d) $\theta = \arctan(1/3)$. (e) Form factor $\mathcal{F}$ as a function of θ and p_2 with fixed $p_1 = 0.5$. (f, g) The localized and delocalized eigenmodes with the largest propagation constant supported by a moiré lattice with $p_1 = 0.5$ and $\theta = \arctan(\sqrt{3}/3)$ for $p_2 = 0.3$ and 0.7, respectively.

lattice is exactly periodic, or commensurate, but for all other angles the moiré lattice is aperiodic, or incommensurate [21].

To realize such a potential within the Rydberg EIT framework, we follow the standard method outlined in Refs. [56–58]. Initially, we consider the half Rabi frequency of the control field as space dependent, denoted as $\Omega_c = \Omega_c(\vec{\zeta})$. Consequently, the optical potential becomes a function of Ω_c. Then, by Taylor expanding $V_{\rm op}$ around $\Omega_c = \Omega_{c0}(\vec{\zeta} = 0)$ to the first order, we derive the expression of the control field with the form

$$\Omega_c(\vec{\zeta}) = \Omega_{c0} + \left(\frac{\partial V_{\rm op}}{\partial \Omega_c}\right)^{-1}\Big|_{\Omega_c=\Omega_{c0}} [V_{\rm op,T} - V(\Omega_{c0})] + O(\epsilon^2), \tag{8}$$

where we set $\Omega_{c0} = 2.0 \times 10^7$. This expression reveals that the distribution of Ω_c is proportional to that of the target moiré potential $V_{\rm op,T}$. Notably, the periodic spatial modulation of the control field is experimentally achievable using a high-resolution spatial light modulator with a pixel size smaller than the probe-beam radius.

B. Localization-delocalization transition

In the subsequent analysis, for the sake of convenience and generality, we set $p_1 = 0.5$ and $p_2 = 0.3$, while varying the twisted angle θ to demonstrate different configurations of the moiré lattice. For instance, we depict the corresponding moiré lattices in Fig. 2 with diverse parameters. Figures 2(a) and 2(c) represent the distribution of the periodic lattice with $\theta = \tan^{-1}(3/4)$ (satisfying $3^2 + 4^2 = 5^2$, known as a Pythagorean triple) and $\theta = \tan^{-1}(5/12)$, respectively. Additionally, Figs. 2(b) and 2(d) exhibit the aperiodic moiré lattices corresponding to $\theta = \tan^{-1}(\sqrt{3}/3)$ and $\tan^{-1}(1/3)$, respectively.

It is evident that when θ satisfies Pythagorean angles, the lattice distribution becomes periodic, and vice versa. Moreover, the characteristics of spatial modes supported by moiré lattices may qualitatively alter with an increase in the depth of one of the sublattices constituting the structure. For convenience, we omit the nonlinear effect in Eq. (6) and assume the linear eigenmodes of the moiré lattice take the form $u = v(\vec{\zeta})\exp(i\mu s)$, where μ denotes the propagation constant. Meanwhile, we define the form factor $\mathcal{F}$ as

$$\mathcal{F} = \frac{(\int |v(\vec{\zeta})|^4 d^2\zeta)^{1/2}}{\int |v(\vec{\zeta})|^2 d^2\zeta} \tag{9}$$

to represent the distribution of the mode, where a highly localized mode will yield a large $\mathcal{F}$ value. Here $v(\vec{\zeta})$ represents the most localized eigenmode with the maximum value $\mu = \mu_{\rm max}$, which varies with the twist angle θ and sublattice depth p_2. Illustrated in Fig. 2(e) is $\mathcal{F}$ as a function of the twist angle θ and sublattice depth p_2. Notably, for non-Pythagorean angles θ, the modes of an aperiodic moiré lattice exhibit a linear LDT and become localized when p_2 exceeds a critical value. Conversely, for Pythagorean angles θ, the eigenmodes remain delocalized regardless of p_2 because in this case the moiré pattern is periodic, as delineated by the dotted white lines in the inset of Fig. 2(e) with $\tan\theta = \frac{3}{4}$ or $\frac{4}{3}$. This phenomenon originates from the suppressed diffraction caused by the flatness of the allowed bands within the effective Pythagorean lattice [19]. Additionally, both localized and delocalized modes are displayed in Fig. 2(f) with $p_1 = 0.5$ and $p_2 = 0.3$ as well as in Fig. 2(g) with $p_1 = 0.5$ and $p_2 = 0.7$.

IV. NUMERICAL STUDY ON THE NONLOCAL OPTICAL SOLITON

A. Modulation instability analysis

Building upon the linear analysis, we now delve into the nonlinear dynamics by incorporating the nonlocal Kerr nonlinearity in Eq. (6). Before proceeding, we carry out

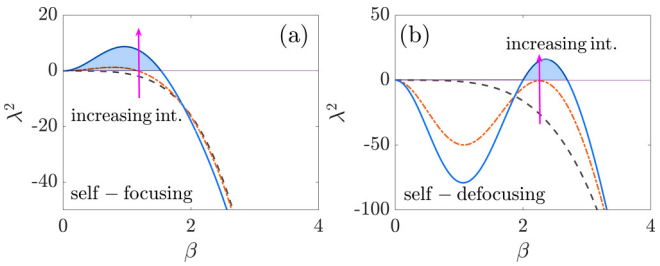

FIG. 3. MI analysis for Eq. (6) under (a) self-focusing and (b) self-defocusing Kerr nonlinearities, where the square of growth rate λ^2 as a function of wave number β by varying the strength of nonlocal interaction. In the plots, dotted black, dashed orange, and solid blue lines (i.e., the direction of the arrow) represent increasing levels of interaction, and blue regions are for the appearance of MI.

the MI analysis, which is a well-known phenomenon in physics [36,37,59]. The main effect of MI is an exponential growth of the modulation amplitude of the constant-amplitude continuous waves under long-wavelength perturbations. This phenomenon occurs in numerous contexts featuring attractive and local cubic nonlinearity, and may also arise in systems with repulsive but nonlocal cubic nonlinearity when perturbations possess both long and short wavelengths.

We first assume the slowly varying potential $V_{\rm op} = 0$ to explore the MI. In this case Eq. (6) has the homogeneous solution $u_{\rm pw} = A_0 \exp(i\mu s)$, where $A_0^2 = 1/\iint d^2\zeta$ and $\mu = -A_0^2 \iint \Re(\vec{\zeta}) d^2\zeta$. The perturbation solution can be expressed as

$$u_p(\vec{\zeta}, s) = [A_0 + u'(\vec{\zeta}, s)]e^{i\mu s}, \tag{10}$$

where $u' = a_1 \exp(i\vec{\beta}\cdot\vec{\zeta} + \lambda s) + a_2^* \exp(-i\vec{\beta}\cdot\vec{\zeta} + \lambda^* s)$ with a_1 and a_2 the small complex amplitudes of the perturbation, $\vec{\beta} = (\beta_1, \beta_2)$, β_1 and β_2 are the nondimensional wave vectors, and λ is the growth rate of the perturbation. Substituting Eq. (10) into Eq. (6) and keeping only linear terms of a_1 and a_2, we obtain

$$\lambda^2 = -\beta^2\left[\beta^2 + 2A_0^2\,\tilde{\Re}(\vec{\beta})\right], \tag{11}$$

where $\beta = (\beta_1^2 + \beta_2^2)^{1/2}$ and $\tilde{\Re}(\vec{\beta})$ is the response function of $\Re(\vec{\zeta})$ in momentum space. Combining the assumption of small complex amplitudes for the perturbation u' with Eq. (11), we observe that when the real part of λ is positive [i.e., $\mathrm{Re}(\lambda) > 0$] the perturbation grows exponentially, leading to the occurrence of MI in the system.

To verify MI, we consider realistic examples using ^{88}Sr and ^{87}Rb atomic gases, respectively. In the case of ^{88}Sr Rydberg atoms, which exhibit attractive interactions corresponding to self-focusing Kerr nonlinearity [53–55], we select the energy levels as follows: $|1\rangle = |5s^2\,{}^1S_0\rangle$, $|2\rangle = |5s5p\,{}^1P_1\rangle$, and $|3\rangle = |5sns\,{}^1S_0\rangle$. On the other hand, for ^{87}Rb Rydberg atoms representing repulsive interactions associated with self-defocusing Kerr nonlinearity [60,61], we assign the atomic levels as $|1\rangle = |5S_{1/2}\rangle$, $|2\rangle = |5P_{3/2}\rangle$, and $|3\rangle = |nS_{1/2}\rangle$. Subsequently, we depict λ^2 as a function of β and the strength of interaction in Fig. 3. In these plots, dotted black, dashed orange, and solid blue lines indicate increasing levels of interaction, while the colored regions represent instability under perturbation. It is suggested from Figs. 3(a) and 3(b) that for self-focusing Kerr nonlinearity, the MI manifests as long-wave instability, whereas for self-defocusing Kerr nonlinearity, it presents as short-wave instability. Regarding the latter, the finite-wavelength (short-wave) instability associated with self-defocusing nonlinearity is fundamentally analogous to the roton instability observed in various atomic gases, as discussed in Refs. [41,46,48].

B. Numerical study on optical solitons

Turning now to the nonlinear regime and basing on the MI analysis, our investigation centers on the formation and propagation of stable solitons through numerical simulations of Eq. (6). To keep the attractive interaction between the Rydberg atoms (i.e., map onto self-focusing Kerr nonlinearity), we consider strontium atom (^{88}Sr) as an example. We look for soliton solutions of Eq. (6) in the form of $u(\vec{\zeta}) = v(\vec{\zeta})\exp(i\mu s)$, where μ the nonlinear propagation constant, which exceeds the propagation constants of the linear eigenmode. Here $v(\vec{\zeta})$ admits the nonlinear eigenvalue equation

$$\mu v = \nabla_\perp^2 v - V_{\rm op}(\vec{\zeta})v - \iint d^2\zeta' \tilde{\Re}(\vec{\zeta}' - \vec{\zeta})|v(\vec{\zeta}', s)|^2 v. \tag{12}$$

This equation can be solved by accelerated imaginary-time evolution method [62]. Meanwhile both the solitary wave and its linear stability can be determined simultaneously by these same imaginary-time iterations.

To the end, we consider the two physical quantities, i.e., the power P and the amplitude $v_{\rm max}$ of the probe laser field, which are defined by

$$P = \iint |v(\vec{\zeta})|^2 d^2\zeta \ \text{ and } \ v_{\rm max} = \max|v|, \tag{13}$$

where $v(\vec{\zeta})$ is the distribution of the beam at the output. We solve Eq. (12) numerically using Gaussian shaped inputs $u_0 = \exp(-\zeta^2)$ as the initial condition, and then find the nonlinear eigenvalue μ by varying the input power. Illustrated in Fig. 4 are the plots of power P (blue) and amplitude $v_{\rm max}$ (red) as functions of μ at different moiré potentials. Here Fig. 4(a) shows P and $v_{\rm max}$ as a function of μ for an incommensurate moiré lattice with rotation angle $\theta = \arctan(\sqrt{3}/3)$, $p_1 = 0.5$, and $p_2 = 0.1$, where p_2 is chosen below the critical value of LDT. We see that the power curve is nonmonotonic with μ and the amplitude decreases drastically in low power since incommensurate moiré lattices have either delocalized or localized linear modes. Such behavior means the soliton can exist only if the input power P exceeds a critical value (e.g., $P_{\rm cr} = 0.03$), below which the beam will diffract. Furthermore, we solve Eq. (12) and plot power P (blue) and amplitude $v_{\rm max}$ (red) as functions of μ for an incommensurate moiré lattice with rotation angle $\theta = \arctan(\sqrt{3}/3)$, $p_1 = 0.5$, and $p_2 = 0.7$, where p_2 is chosen above the critical value of LDT in Fig. 4(b). We see that the power curve is monotonic with μ and hence the input beam is well localized at any power P since the linear localized mode exists. Therefore, there is no critical value for soliton power.

In addition, we further simulate and then plot power P (blue) and amplitude $v_{\rm max}$ (red) as functions of μ for a

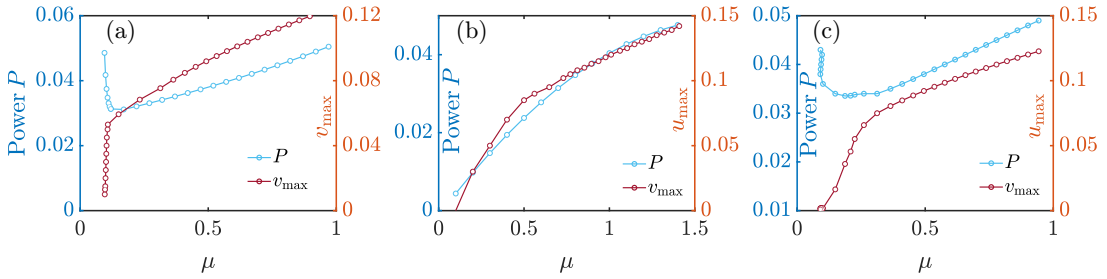

FIG. 4. Beam power P (blue line) and amplitude $v_{\max}$ (red line) as functions of μ for an incommensurate moiré lattice with rotation angle $\theta = \arctan(\sqrt{3}/3)$, $p_1 = 0.5$, and (a) $p_2 = 0.1$ (below the critical value of LDT) and (b) $p_2 = 0.7$ (above the critical value of LDT), and for (c) a commensurate moiré lattice with rotation angle $\theta = \arctan(3/4)$, $p_1 = 0.5$, and $p_2 = 0.7$.

commensurate moiré lattice with rotation angle $\theta = \arctan(4/3)$, $p_1 = 0.5$, and $p_2 = 0.7$ in Fig. 4(c). It shows that the curve is similar in behavior to the incommensurate moiré lattice for the condition of p_2 below the critical value. However, there exists a power threshold for any p_2 since the linear mode is always delocalized for an incommensurate moiré lattice. Based on the analysis above, we further solve Eq. (12) under different initial conditions to explore high-order soliton solutions. We first choose the HG mode as the initial condition:

$$u_{m,n}(\vec{\zeta}) = H_n(\sqrt{2}\xi)H_m(\sqrt{2}\eta)\exp(-\zeta^2). \tag{14}$$

We begin by setting $m = 1$ and $n = 0$. The depths of the moiré potential and rotation angle are chosen as $p_1 = 0.5$, $p_2 = 1$, and $\theta = \arctan(\sqrt{3}/3)$, which is corresponding to a localized linear mode in Fig. 2(e). The top row of Figs. 5(a1)–5(a5) illustrates the intensity distribution $|u|^2$ of HG solitons as functions of ξ and η for propagation distances $s = 0$, 2, 4, 6, and 8. Notably, the intensity of the soliton remains stable during propagation, albeit the two peaks exhibit rotation around their center. Moreover, with extended simulation time, we observe that the soliton pair remains stable while being movable across the entire space, although these results are not depicted here. Subsequently, we conduct further numerical simulations with $m = n = 1$ and keep other parameters fixed, resulting in higher-order stable solitons. The intensity $|u|^2$ as a function of ξ and η is illustrated in the bottom row of Figs. 5(b1)–5(b5). These solitons exhibit exceptional stability during propagation and demonstrate mobility and rotation.

The behaviors of movable and rotatable solitons may be attributed to two fundamental factors: first, 2D bright solitons, inherently endowed with vorticity, can attain a remarkable degree of stability; second, the soliton's mobility within the lattice is contingent upon the intensity of the probe field. Specifically, when the intensity remains below a critical threshold, the soliton traverses the lattice unhindered. Conversely, exceeding this threshold leads to the soliton becoming entrapped within the intricate moiré potential. These solitons are prevalent across a wide range of physical phenomena, as demonstrated in the research of Sakaguchi and Malomed [63,64], Christodoulides *et al.* [65], Yang and Musslimani [66], etc.

Additionally, stable vortex solutions of Eq. (12) can be found through numerical simulations. For instance, one may utilize the LG mode as the input:

$$u(\vec{\zeta}) = C_{\mathrm{mp}}(\sqrt{2}|\zeta|)^{|m|}\exp(-\zeta^2)L_{\mathrm{p}}^{|m|}(2\zeta^2)\exp(-im\phi), \tag{15}$$

where $C_{\mathrm{mp}} = (\frac{2p!}{\pi(p+|m|)!})^{1/2}$, $L_{\mathrm{p}}^{|m|}(\cdot)$ represents a generalized LG polynomial with m denoting the azimuthal index and p the radial index, a signifies the beam waist, and $\phi = \arctan(\eta/\xi)$ stands for the azimuthal angle.

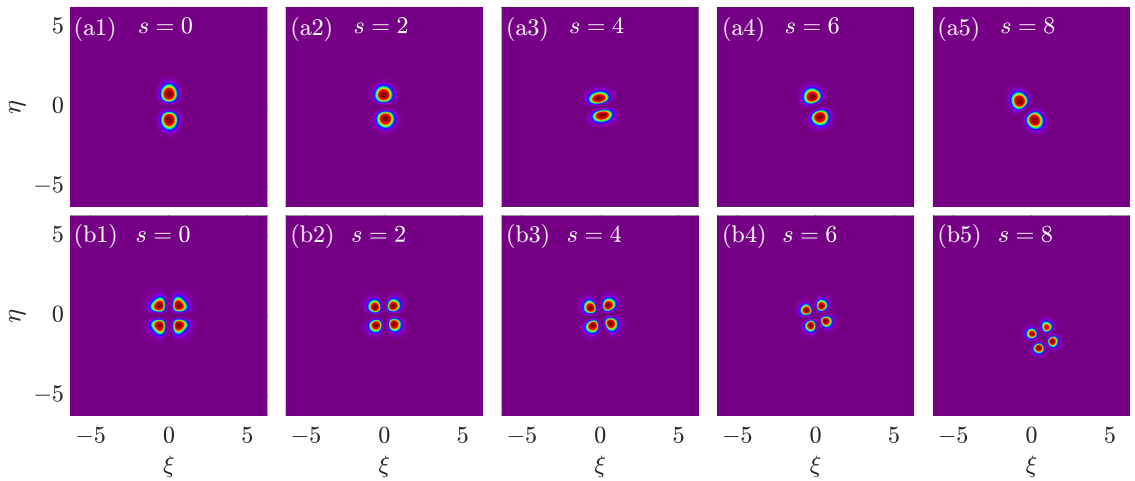

FIG. 5. Intensity distribution of the HG solitons $|u|^2$ as functions of ξ and η for different propagation distance $s = 0$, 2, 4, 6, and 8. Here the initial conditions $u_{n,m}(\vec{\zeta})$ are respectively for $(n = 0, m = 1)$ in the top row and for $(n = 1, m = 1)$ in the bottom row.

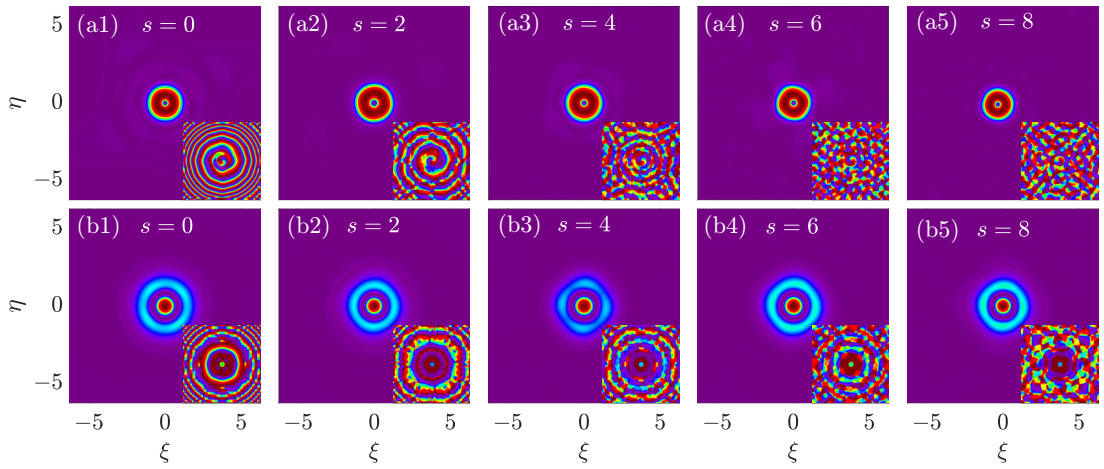

FIG. 6. Intensity ($|u|^2$) and phase distributions of the LG solitons as functions of ξ and η for different propagation distance $s = 0, 2, 4, 6$, and 8. Here the initial conditions are given in Eq. (15) respectively for $(p = 0, m = 1)$ in the top row and for $(p = 1, m = 0)$ in the bottom row.

To illustrate, we provide two examples of stable vortex solutions. First, we solve Eq. (6) for $p = 0$ and $m = 1$. The intensity distribution $|u|^2$ as functions of ξ and η for propagation distances $s = 0, 2, 4, 6$, and 8 is depicted in the top row of Fig. 6. Additionally, we calculate the phase distribution u inset in each panel. Notably, the amplitude of vortices remains stable during propagation, but the phase changes with propagating. As a second example, we conduct a numerical simulation on Eq. (6) with $p = 1$ and $m = 0$. The corresponding simulation results are presented in the bottom row of Fig. 6. Compared with the two scenarios, it shows that the $(p, m) = (0, 1)$ vortex featuring a single vortex circulation around the center with a fundamental radial mode is much more stable than the $(p, m) = (1, 0)$ vortex, exhibiting a radial node without vortex circulation. For the high-order LG modes, the intensity may not keep its shape under the current conditions. The physical reason for the stability of the $(2 + 1)$D soliton and vortices obtained here is the strong and long-range nonlocal Kerr nonlinearity coming from the Rydberg-Rydberg interaction between atoms as well as the moiré lattice potential, which not only can suppress the diffraction in transverse directions but also can arrest the spread or collapse of high-dimensional nonlinear optical beams.

V. OPTICAL PATTERN FORMATIONS AND THEIR STRUCTURAL TRANSITIONS

In the previous section, it was noted that short-wave modulation instability occurs when nonlocal interaction is repulsive, leading to the formation of extended structures. To explore this phenomenon further, we choose to use ^{87}Rb Rydberg atoms, which exhibit repulsive interactions consistent with self-defocusing Kerr nonlinearity. We also notice that there exist various interactions including the diffraction interaction, the linear interaction from the moiré potential [by the depth of potential (p_1 and p_2), the rotation angle (θ), and lattice constant (a)], and the nonlocal nonlinearity from Rydberg interaction, which is represented by the effective strength of interaction $\alpha = A_0^2 \iint \Re(\vec{\zeta}) d^2\zeta$.

Based on these considerations and in order to obtain ground-state patterns, we use numerical simulations to seek the ground-state solution of the system. This involves solving Eq. (6) through an imaginary-time evolution method and the split-step Fourier method. The approach ensures that the total energy of the system

$$E = \int |\tilde{\nabla}_\perp u(\vec{\zeta}, s)|^2 d^2\zeta + \int V_{\rm op}(\vec{\zeta}) |u(\vec{\zeta}, s)|^2 d^2\zeta' + \frac{1}{2} \iint \Re(\vec{\zeta}' - \vec{\zeta}) |u(\vec{\zeta}, s)|^2 |u(\vec{\zeta}', s)|^2 d^2\zeta' d^2\zeta \quad (16)$$

is minimized. This allows for the efficient extraction of the ground-state properties of the system and aids in the exploration of optical pattern formation.

As a first step, we focus on the case of pattern formation controlled by the strength of nonlinear interaction α. Figure 7 presents the distributions of $|u|^2$ as functions of ξ and η for varying values α of nonlocal nonlinear strength, while keeping the moiré potential constant (e.g., with $p_1 = 2.5$, $p_2 = 3.5$, and lattice constant $a = 2$). Specifically, the values of α are chosen as 0.1, 1, 5, 15, 30, 40, 50, and 100 in Figs. 7(a)–1(h), respectively. Additionally, we also plot the distribution of moiré potential $V_{\rm op}(\xi, \eta)$ as a function of ξ and η in Fig. 7(i). The figures reveal that the ground state is basically trapped by the lattice potential when nonlocal nonlinear strength α is small [i.e., Figs. 7(a) and 7(b)]. The ring patterns nested in the square patterns appear when α increases [i.e., Figs. 7(c) and 7(d)]. The ring structures begin to merge with square patterns and then transit into four droplet structures when α increases further [i.e., Figs. 7(e) and 7(f)]. At very high values of α [e.g., Figs. 7(g) and 7(h)], all patterns evolve into hexagonal droplet structures.

By keeping the effective strength of interaction α fixed and varying the moiré lattice constant a, we can further explore the optical patterns. Figure 8 illustrates the distributions of $|u|^2$ as functions of ξ and η for different values of moiré lattice constant a, while maintaining $\alpha = 40$. The chosen values of a in Figs. 8(a)–8(h) are 0.5, 1.5, 2, 2.7, 2.9, 3.5, 4.3, and 5, respectively.

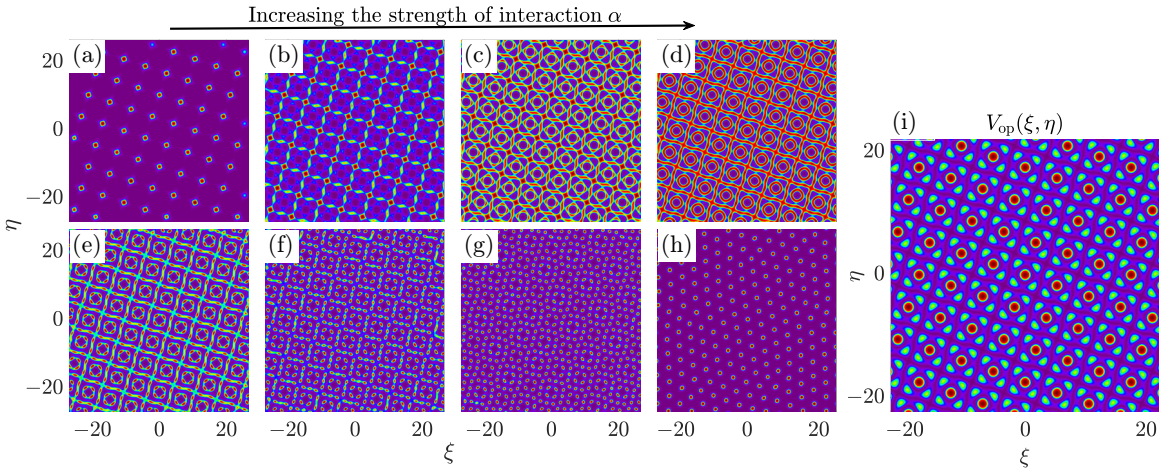

FIG. 7. Distributions of $|u|^2$ as functions of ξ and η for various pattern formations within different values α of nonlocal nonlinear strength: (a) $\alpha = 0.1$, (b) $\alpha = 1$, (c) $\alpha = 5$, (d) $\alpha = 15$, (e) $\alpha = 30$, (f) $\alpha = 40$, (g) $\alpha = 50$, and (h) $\alpha = 100$. (i) Distribution of moiré potential $V_{\rm op}(\xi, \eta)$ as a function of ξ and η at $p_1 = 2.5$, $p_2 = 3.5$, and lattice constant $a = 2$. In all panels, large values are indicated by red colors, while small values are represented by purple colors.

When the lattice constant a is small, such as in Fig. 8(a), multilayer annular structures emerge. As a increases to 1.5 in Fig. 8(b), the annular structures transition into polygonal forms. In Fig. 7(c), increasing α to 2 leads to a shift from polygonal structures to square-shaped droplet structures. These then merge completely into droplet structures, as depicted in Figs. 8(d) and 8(e). Hexagonal structures begin to appear when a reaches 3.5. At very high values of a [e.g., Figs. 7(g) and 7(h)], all patterns evolve into square structures.

Comparing all panels in Fig. 8, we observe that as a increases, the distance between the peaks of the droplets also increases. Furthermore, the patterns undergo a structural phase transition from multilayer annular structures to polygonal structures, square-shaped droplet structures, droplet structures, hexagonal structures, and finally square structures. This analysis demonstrates that the interplay between the linear moiré potential and nonlinear interaction (nonlinear potential) leads to the breaking of translational symmetry, resulting in the emergence of various ground-state patterns.

VI. SUMMARY

In conclusion, we investigate the optical nonlinear dynamics within a system of Rydberg atoms exhibiting a ladder-type EIT configuration, subjected to a moiré lattice potential. By incorporating nonlocal Kerr nonlinearity stemming from Rydberg-Rydberg interactions and designing the optical moiré lattice, we show the condition for formation and propagation of stable solitons, vortices, and optical pattern formations in the commensurate and incommensurate moiré lattice, respectively. Through MI analysis and numerical simulations, we find that HG and LG solitons and vortices exhibit excep-

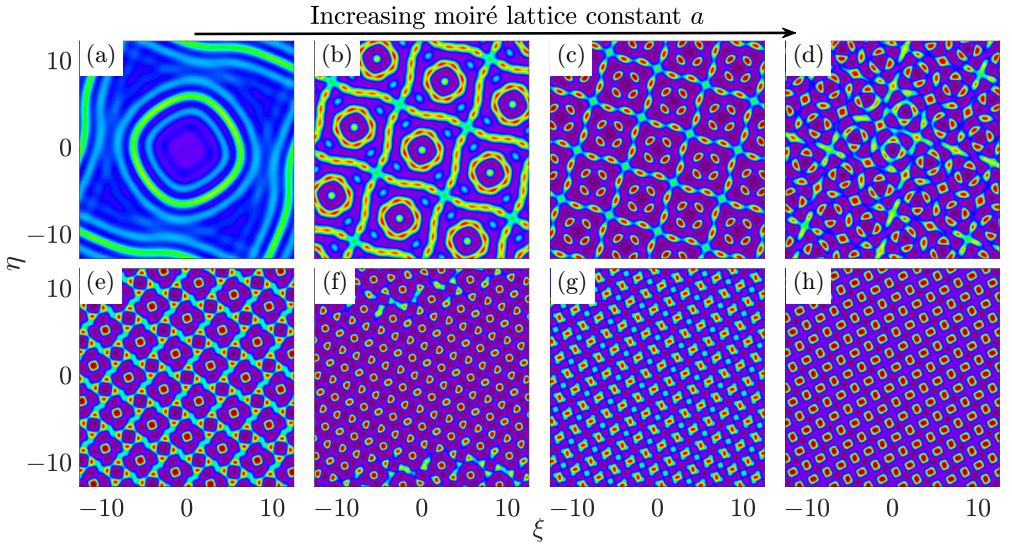

FIG. 8. Distributions of $|u|^2$ as functions of ξ and η for various pattern formations within different moiré lattice constant a: (a) $a = 0.5$, (b) $a = 1.5$, (c) $a = 2$, (d) $a = 2.7$, (e) $a = 2.9$, (f) $a = 3.5$, (g) $a = 4.3$, and (h) $a = 5$. In all panels, large values are indicated by red colors, while small values are represented by purple colors.

tional stability and mobility for self-focusing Kerr nonlinearity. In contrast, our simulations reveal the emergence of various extended structures for self-defocusing Kerr nonlinearity. Additionally, we observe various structural phase transitions in the optical patterns by varying the moiré lattice constant and the strength of nonlinear interaction. Our paper provides a versatile platform for manipulating and controlling light-matter interactions in Rydberg atomic ensembles, which leads to the breaking of translational symmetry and the emergence of diverse ground-state patterns. These advancements can have applications in areas such as optical computing, information processing, and the creation of novel optical devices.

ACKNOWLEDGMENTS

Z.S. acknowledges the support of National Natural Science Foundation of China (Grant No. 12304357), Hubei Provincial Natural Science Foundation of China (Grant No. 2023AFB352), the start-up fund project of Hubei University of Automotive Technology (Grant No. BK202210), Hubei Province Higher Education Excellent Young and Middle Aged Science and Technology Innovation Team Plan Project Grant No. T2023012, and Shiyan Key Laboratory of Quantum Information and Precision Optics (Hubei University of Automotive Technology) with Grant No. SYZDK12024A02. Y. Zhou acknowledges the support of Hubei Provincial Natural Science Foundation of China (Grant No. 2023AFB891) and Chunhui Project Foundation of the Education Department of China (Grant No. HZKY20220337). L.Q. acknowledges the support of National Natural Science Foundation of China (Grant No. 12247146). Y. Zhong acknowledges the support of Hubei Provincial Natural Science Foundation of China (Grant No. 2024AFB1043) and the startup fund project of Hubei University of Automotive Technology (Grant No. BK202308).

APPENDIX: BLOCH EQUATIONS AND THEIR SOLUTIONS FOR DENSITY-MATRIX ELEMENTS

1. Bloch equation for one-body density-matrix elements

The explicit expression of the optical Bloch equation (2) for one-body density-matrix elements $\rho_{\alpha\beta}$ is given by

$$i\frac{\partial}{\partial t}\rho_{11} - i\Gamma_{12}\rho_{22} - \Omega_p\rho_{12} + \Omega_p^*\rho_{21} = 0, \tag{A1a}$$

$$i\frac{\partial}{\partial t}\rho_{22} - i\Gamma_{23}\rho_{33} + i\Gamma_{12}\rho_{22} + (\Omega_p\rho_{12} + \Omega_c^*\rho_{32} + \text{c.c.}) = 0, \tag{A1b}$$

$$i\frac{\partial}{\partial t}\rho_{33} + i\Gamma_{23}\rho_{33} + \Omega_c\rho_{23} - \Omega_c^*\rho_{32} = 0, \tag{A1c}$$

$$\left(i\frac{\partial}{\partial t} + d_{21}\right)\rho_{21} - \Omega_p(\rho_{22} - \rho_{11}) + \Omega_c^*\rho_{31} = 0, \tag{A1d}$$

$$\left(i\frac{\partial}{\partial t} + d_{31}\right)\rho_{31} - \Omega_p\rho_{32} + \Omega_c\rho_{21} - \frac{\mathcal{N}_a}{2}\int d^3r'\mathcal{V}_{\text{vdW}}(\mathbf{r}' - \mathbf{r})\rho_{33,31}(\mathbf{r}', \mathbf{r}, t) = 0, \tag{A1e}$$

$$\left(i\frac{\partial}{\partial t} + d_{32}\right)\rho_{32} - \Omega_p^*\rho_{31} - \Omega_c(\rho_{33} - \rho_{22}) - \frac{\mathcal{N}_a}{2}\int d^3r'\mathcal{V}_{\text{vdW}}(\mathbf{r}' - \mathbf{r})\rho_{33,32}(\mathbf{r}', \mathbf{r}, t) = 0. \tag{A1f}$$

Here $d^3r' = dx'dy'dz'$; $d_{\alpha\beta} = \Delta_\alpha - \Delta_\beta + i\gamma_{\alpha\beta}$ $(\alpha, \beta = 1, 2, 3; \alpha \neq \beta)$; $\Delta_2 = \omega_p - (\omega_2 - \omega_1)$ and $\Delta_3 = \omega_p + \omega_c - (\omega_3 - \omega_2)$, are respectively one- and two-photon detunings; $\gamma_{\alpha\beta} = (\Gamma_\alpha + \Gamma_\beta)/2 + \gamma_{\alpha\beta}^{\text{dep}}$ with $\Gamma_\alpha = \sum_{\alpha<\beta}\Gamma_{\alpha\beta}$ ($\Gamma_{\alpha\beta}$ and $\gamma_{\alpha\beta}^{\text{dep}}$ are the spontaneous emission decay rate and dephasing rate from $|\beta\rangle$ to $|\alpha\rangle$, respectively). From the left-hand side of the above equations, we observe that unlike conventional EIT, there are additional terms arising from the Rydberg-Rydberg interaction in Eqs. (A1e) and (A1f), which involves the van der Waals interaction between two atoms positioned at $\mathbf{r}'$ and $\mathbf{r}$ excited to the same Rydberg states.

While the equations above describe the time evolution of the one-body density-matrix elements $\rho_{\alpha\beta}(\mathbf{r}, t)$, they also involve two-body DM elements $\rho_{\alpha\beta,\mu\nu}(\mathbf{r}', \mathbf{r}, t) = \langle\hat{S}_{\alpha\beta}(\mathbf{r}', t)\hat{S}_{\mu\nu}(\mathbf{r}, t)\rangle$ due to the Rydberg-Rydberg interaction. Likewise, the equations of motion for the two-body DM elements (not shown here for brevity) involve three-body DM elements, and so on. Solving such a complex many-body problem requires a suitable truncation of the infinite equation chain related to many-body correlations, along with a self-consistent calculation that goes beyond the mean-field approximation. These advanced methods have been developed recently [52].

2. Solutions for density-matrix elements

In this paper, we focus on the stationary states of the system. As such, the time derivatives in the MB equations (A1) can be neglected (i.e., $\partial/\partial t = 0$), which is a valid assumption when the probe and control fields have a long duration. To proceed, we adopt the method developed in Refs. [52] to first solve the Bloch equation (A1) under the condition of Rydberg EIT. We assume that all atoms are initially prepared in the ground state $|1\rangle$. Given the weak intensity of the probe field, we use $\Omega_p \sim \varepsilon$ as the expansion parameter, allowing us to expand the density-matrix elements as $\rho_{\alpha\beta} = \varepsilon\rho_{\alpha\beta}^{(1)} + \varepsilon^2\rho_{\alpha\beta}^{(2)} + \ldots$ for the combinations $(\beta = 1, 2; \alpha = 2, 3; \beta < \alpha)$. By substituting these expansions into Eq. (A1) and collecting coefficients of ε^l $(l = 0, 1, 2, \ldots)$, we obtain a series of linear but inhomogeneous equations that can be solved order by order.

The first-order solution reads

$$\rho_{21}^{(1)} = \frac{d_{31}}{D}\Omega_p \equiv a_{21}^{(1)}\Omega_p, \tag{A2}$$

$$\rho_{31}^{(1)} = -\frac{\Omega_c}{D}\Omega_p, \tag{A3}$$

where $D = |\Omega_c|^2 - d_{21}d_{31}$. The second order solution is

$$\rho_{11}^{(2)} = \frac{[i\Gamma_{23} - 2|\Omega_c|^2M]N - i\Gamma_{12}P}{-\Gamma_{12}\Gamma_{23} - i\Gamma_{12}|\Omega_c|^2M}, \tag{A4}$$

$$\rho_{33}^{(2)} = \frac{N}{i\Gamma_{12}} - \rho_{11}^{(2)}, \tag{A5}$$

$$\rho_{32}^{(2)} = \frac{\Omega_c}{d_{32}}\left(2\rho_{33}^{(2)} + \rho_{11}^{(2)} - \frac{1}{D}\right), \tag{A6}$$

where $M = 1/d_{32} - 1/d_{32}^*$, $N = d_{31}^*/D^* - d_{31}/D$, and $P = \frac{|\Omega_c|^2}{D^* d_{32}^*} - \frac{|\Omega_c|^2}{D d_{32}}$. The third-order solution is given by

$$\rho_{21}^{(3)} = a_{21,1}^{(3)} |\Omega_p|^2 \Omega_p + a_{21,2}^{(3)} \mathcal{N}_a \int d^3\mathbf{r}' \mathcal{V}_{\text{vdW}}(\mathbf{r}' - \mathbf{r}) \rho_{33,31}^{(3)}(\mathbf{r}' - \mathbf{r}), \tag{A7}$$

where $a_{21,1}^{(3)} = \frac{\Omega_c^*}{D}\rho_{32}^{(2)} + \frac{d_{31}}{D}(2\rho_{11}^{(2)} + \rho_{33}^{(2)})$ and $a_{21,2}^{(3)} = \frac{\Omega_c^*}{D}$.

We observe that the two-body density-matrix element $\rho_{33,31}^{(3)}$ needs to be calculated concurrently with $\rho_{21}^{(3)}$ as described in Eq. (A7). Upon a straightforward examination of the magnitude of the two-body density-matrix elements $\rho_{\alpha\beta,\mu\nu}$ under the weak EIT condition, we begin the expansion of $\rho_{\alpha\beta,\mu\nu}$ from the order of ε^2. Thus, we express the expansion as follows: $\rho_{\alpha\beta,\mu\nu} = \varepsilon^2 \rho_{\alpha\beta,\mu\nu}^{(2)} + \varepsilon^3 \rho_{\alpha\beta,\mu\nu}^{(3)} + \ldots$. This expansion leads to the following two-body equation for second order:

$$\begin{pmatrix} d_{21} & 0 & \Omega_c^* \\ 0 & d_{31} - \mathcal{V}_{\text{vdW}}/2 & \Omega_c \\ \Omega_c & \Omega_c^* & d_{21} + d_{31} \end{pmatrix} \begin{pmatrix} \rho_{21,21}^{(2)} \\ \rho_{31,31}^{(2)} \\ \rho_{31,21}^{(2)} \end{pmatrix} = \begin{pmatrix} -\frac{d_{31}}{D} \\ 0 \\ \frac{\Omega_c}{D} \end{pmatrix} |\Omega_p|^2. \tag{A8}$$

The solution is of the form

$$\rho_{\alpha\beta,\mu\nu}^{(2)} = a_{\alpha\beta,\mu\nu}^{(2)} |\Omega_p|^2, \tag{A9}$$

with $\{\alpha\beta, \mu\nu\} = \{21, 21\}, \{31, 31\}$ and $\{21, 31\}$. Additionally, other two-body equations for second order can also be derived using the relation $\rho_{\alpha\beta,\mu\nu}^{(2)} \equiv \rho_{\alpha\beta}^{(1)} \rho_{\mu\nu}^{(1)}$ for $\{\alpha\beta, \mu\nu\} = \{21, 12\}, \{31, 13\}$, and $\{21, 13\}$. These equations do not involve the term $\mathcal{V}_{\text{vdW}}$ and can be derived by combining the first-order density-matrix elements as indicated by the relation.

The third-order equations for the two-body density-matrix elements $\rho_{\alpha\beta,\mu\nu}^{(3)}$ can be addressed by solving the equations provided, which yield solutions of the form

$$\rho_{\alpha\beta,\mu\nu}^{(3)} = a_{\alpha\beta,\mu\nu}^{(3)} |\Omega_p(\mathbf{r}', t)|^2 \Omega_p(\mathbf{r}, t), \tag{A10}$$

where $a_{\alpha\beta,\mu\nu}^{(3)}$ are functions of the system parameters. Here $\rho_{\alpha\beta,\mu\nu}^{(3)}$ satisfies

$$\begin{pmatrix} i\Gamma_{12} + d_{21} & \Omega_c^* & -i\Gamma_{23} & 0 & \Omega_c^* & -\Omega_c & 0 & 0 \\ \Omega_c & i\Gamma_{12} + d_{31} & 0 & -i\Gamma_{23} & 0 & 0 & \Omega_c^* & -\Omega_c \\ 0 & 0 & i\Gamma_{23} + d_{21} & \Omega_c^* & -\Omega_c^* & \Omega_c & 0 & 0 \\ 0 & 0 & \Omega_c & \mathcal{M}_1 & 0 & 0 & -\Omega_c^* & \Omega_c \\ \Omega_c & 0 & -\Omega_c & 0 & d_{32} + d_{21} & 0 & \Omega_c^* & 0 \\ -\Omega_c^* & 0 & \Omega_c^* & 0 & 0 & d_{23} + d_{21} & 0 & \Omega_c^* \\ 0 & \Omega_c & 0 & -\Omega_c & \Omega_c & 0 & \mathcal{M}_2 & 0 \\ 0 & -\Omega_c^* & 0 & \Omega_c^* & 0 & \Omega_c & 0 & d_{23} + d_{31} \end{pmatrix} \begin{pmatrix} \rho_{22,21}^{(3)} \\ \rho_{22,31}^{(3)} \\ \rho_{33,21}^{(3)} \\ \rho_{33,31}^{(3)} \\ \rho_{32,21}^{(3)} \\ \rho_{21,23}^{(3)} \\ \rho_{32,31}^{(3)} \\ \rho_{31,23}^{(3)} \end{pmatrix}$$

$$= \begin{pmatrix} a_{21,21}^{(2)} - a_{21,12}^{(2)} - a_{22}^{(2)} \\ a_{21,31}^{(2)} - a_{31,12}^{(2)} \\ -a_{33}^{(2)} \\ 0 \\ a_{21,31}^{(2)} - a_{32}^{(2)} \\ -a_{32}^{*(2)} - a_{21,13}^{(2)} \\ a_{31,31}^{(2)} \\ -a_{31,13}^{(2)} \end{pmatrix} |\Omega_p(\mathbf{r}')|^2 \Omega_p(\mathbf{r}, t) \tag{A11}$$

where $\mathcal{M}_1 = d_{31} + i\Gamma_{23} - \mathcal{V}_{\text{vdW}}/2$ and $\mathcal{M}_2 = d_{32} + d_{31} - \mathcal{V}_{\text{vdW}}/2$. The solution $\rho_{33,31}^{(3)}$ can be obtained from the above equation, which reads

$$\rho_{33,31}^{(3)} = a_{33,31}^{(3)} |\Omega_p(\mathbf{r}')|^2 \Omega_p(\mathbf{r}, t), \tag{A12}$$

where $a_{33,31}^{(3)}$ is the function of the system parameters, such as $\Gamma_{\alpha\beta}$, Δ_α, and control laser Ω_c.

[1] M. Fleischhauer, A. Imamoğlu, and J. P. Marangos, Electromagnetically induced transparency: Optics in coherent media, Rev. Mod. Phys. **77**, 633 (2005).

[2] M. Saffman, T. G. Walker, and K. Mølmer, Quantum information with Rydberg atoms, Rev. Mod. Phys. **82**, 2313 (2010).

[3] C. S. Adams, J. D. Pritchard, and J. P. Shaffer, Rydberg atom quantum technologies, J. Phys. B **53**, 012002 (2019).

[4] A. K. Mohapatra, T. R. Jackson, and C. S. Adams, Coherent optical detection of highly excited Rydberg states using electromagnetically induced transparency, Phys. Rev. Lett. **98**, 113003 (2007).

[5] J. D. Pritchard, D. Maxwell, A. Gauguet, K. J. Weatherill, M. P. A. Jones, and C. S. Adams, Cooperative atom-light interaction in a blockaded Rydberg ensemble, Phys. Rev. Lett. **105**, 193603 (2010).

[6] O. Firstenberg, C. S. Adams, and S. Hofferberth, Nonlinear quantum optics mediated by Rydberg interactions, J. Phys. B **49**, 152003 (2016).

[7] C. Murray and T. Pohl, Quantum and nonlinear optics in strongly interacting atomic ensembles, in *Advances in Atomic, Molecular, and Optical Physics* (Academic, New York, 2016), Vol. 65, Chap. 7, pp. 321–372.

[8] O. Firstenberg, T. Peyronel, Q.-Y. Liang, A. V. Gorshkov, M. D. Lukin, and V. Vuletic, Attractive photons in a quantum nonlinear medium, Nature (London) **502**, 71 (2013).

[9] H. Bernien, S. Schwartz, A. Keesling, H. Levine, A. Omran, H. Pichler, S. Choi, A. S. Zibrov, M. Endres, M. Greiner, V. Vuletic, and M. D. Lukin, Probing many-body dynamics on a 51-atom quantum simulator, Nature (London) **551**, 579 (2017).

[10] M. Jing, Y. Hu, J. Ma, H. Zhang, L. Zhang, L. Xiao, and S. Jia, Atomic superheterodyne receiver based on microwave-dressed Rydberg spectroscopy, Nat. Phys. **16**, 911 (2020).

[11] H. Busche, P. Huillery, S. W. Ball, T. Ilieva, M. P. A. Jones, and C. S. Adams, Contactless nonlinear optics mediated by long-range Rydberg interactions, Nat. Phys. **13**, 655 (2017).

[12] L. Li and A. Kuzmich, Quantum memory with strong and controllable Rydberg-level interactions, Nat. Commun. **7**, 13618 (2016).

[13] C. L. Degen, F. Reinhard, and P. Cappellaro, Quantum sensing, Rev. Mod. Phys. **89**, 035002 (2017).

[14] T. F. Gallagher, *Rydberg Atoms* (Springer, New York, 2006).

[15] F. Maucher, T. Pohl, S. Skupin, and W. Krolikowski, Self-organization of light in optical media with competing nonlinearities, Phys. Rev. Lett. **116**, 163902 (2016).

[16] S. Sevinçli, N. Henkel, C. Ates, and T. Pohl, Nonlocal nonlinear optics in cold Rydberg gases, Phys. Rev. Lett. **107**, 153001 (2011).

[17] A. K. Geim and I. V. Grigorieva, Van der Waals heterostructures, Nature (London) **499**, 419 (2013).

[18] K. S. Novoselov, A. Mishchenko, A. Carvalho, and A. H. C. Neto, 2D materials and van der Waals heterostructures, Science **353**, aac9439 (2016).

[19] Q. Fu, P. Wang, C. Huang, Y. V. Kartashov, L. Torner, V. V. Konotop, and F. Ye, Optical soliton formation controlled by angle twisting in photonic moiré lattices, Nat. Photonics **14**, 663 (2020).

[20] P. Wang, Y. Zheng, X. Chen, C. Huang, Y. V. Kartashov, L. Torner, V. V. Konotop, and F. Ye, Localization and delocalization of light in photonic moiré lattices, Nature (London) **577**, 42 (2020).

[21] Y. V. Kartashov, F. Ye, V. V. Konotop, and L. Torner, Multifrequency solitons in commensurate-incommensurate photonic moire lattices, Phys. Rev. Lett. **127**, 163902 (2021).

[22] Y. Cao, V. Fatemi, A. Demir, S. Fang, S. L. Tomarken, J. Y. Luo, J. D. Sanchez-Yamagishi, K. Watanabe, T. Taniguchi, E. Kaxiras, R. C. Ashoori, and P. Jarillo-Herrero, Correlated insulator behaviour at half-filling in magic-angle graphene superlattices, Nature (London) **556**, 80 (2018).

[23] Y. Cao, V. Fatemi, S. Fang, K. Watanabe, T. Taniguchi, E. Kaxiras, and P. Jarillo-Herrero, Unconventional superconductivity in magic-angle graphene superlattices, Nature (London) **556**, 43 (2018).

[24] C. R. Dean, L. Wang, P. Maher, C. Forsythe, F. Ghahari, Y. Gao, J. Katoch, M. Ishigami, P. Moon, M. Koshino, T. Taniguchi, K. Watanabe, K. L. Shepard, J. Hone, and P. Kim, Hofstadter's butterfly and the fractal quantum Hall effect in moire superlattices, Nature (London) **497**, 598 (2013).

[25] X. Lin, Z. Liu, T. Stauber, G. Gomez-Santos, F. Gao, H. Chen, B. Zhang, and T. Low, Chiral plasmons with twisted atomic bilayers, Phys. Rev. Lett. **125**, 077401 (2020).

[26] B. Lou, N. Zhao, M. Minkov, C. Guo, M. Orenstein, and S. Fan, Theory for twisted bilayer photonic crystal slabs, Phys. Rev. Lett. **126**, 136101 (2021).

[27] Z. Meng, L. Wang, W. Han, F. Liu, K. Wen, C. Gao, P. Wang, C. Chin, and J. Zhang, Atomic Bose-Einstein condensate in twisted-bilayer optical lattices, Nature (London) **615**, 231 (2023).

[28] Y. V. Kartashov, Light bullets in moire lattices, Opt. Lett. **47**, 4528 (2022).

[29] Z. Chen, X. Liu, and J. Zeng, Electromagnetically induced moire optical lattices in a coherent atomic gas, Front. Phys. **17**, 42508 (2022).

[30] C. Wu, Q. Wan, C. Peng, S. Mo, R. Li, K. Zhao, Y. Guo, S. Yuan, F. Wu, C. Zhang, and N. Xu, Tailoring Dirac fermions by in-situ tunable high-order moire pattern in graphene-monolayer xenon heterostructure, Phys. Rev. Lett. **129**, 176402 (2022).

[31] J. Lee, K.-H. Jin, A. Catuneanu, A. Go, J. Jung, C. Won, S.-W. Cheong, J. Kim, F. Liu, H.-Y. Kee, and H. W. Yeom, Honeycomb-lattice Mott insulator on tantalum disulphide, Phys. Rev. Lett. **125**, 096403 (2020).

[32] F. He, Y. Zhou, Z. Ye, S.-H. Cho, J. Jeong, X. Meng, and Y. Wang, Moire patterns in 2D materials: A review, ACS Nano **15**, 5944 (2021).

[33] Y. S. Kivshar and G. P. Agrawal, *Optical Solitons: From Fibers to Photonic Crystals* (Academic, New York, 2003).

[34] M. C. Cross and P. C. Hohenberg, Pattern formation outside of equilibrium, Rev. Mod. Phys. **65**, 851 (1993).

[35] C. Bowman and A. C. Newell, Natural patterns and wavelets, Rev. Mod. Phys. **70**, 289 (1998).

[36] V. E. Zakharov and L. A. Ostrovsky, Modulation instability: The beginning, Physica D **238**, 540 (2009).

[37] W. Krolikowski, O. Bang, J. J. Rasmussen, and and J. Wyller, Modulational instability in nonlocal nonlinear Kerr media, Phys. Rev. E **64**, 016612 (2001).

[38] J. Wyller, W. Krolikowski, O. Bang, and J. J. Rasmussen, Generic features of modulational instability in nonlocal Kerr media, Phys. Rev. E **66**, 066615 (2002).

[39] W. Królikowski, O. Bang, N. I. Nikolov, D. Neshev, J. Wyller, J. J. Rasmussen, and D. Edmundson, Modulational instability,

solitons and beam propagation in spatially nonlocal nonlinear media, J. Opt. B **6**, S288 (2004).

[40] E. V. Doktorov and M. A. Molchan, Modulational instability in nonlocal Kerr-type media with random parameters, Phys. Rev. A **75**, 053819 (2007).

[41] N. Henkel, R. Nath, and T. Pohl, Three-dimensional roton excitations and supersolid formation in Rydberg-excited Bose-Einstein condensates, Phys. Rev. Lett. **104**, 195302 (2010).

[42] B. K. Esbensen, A. Wlotzka, M. Bache, O. Bang, and W. Krolikowski, Modulational instability and solitons in nonlocal media with competing nonlinearities, Phys. Rev. A **84**, 053854 (2011).

[43] L. Tiofack, H. Tagwo, O. Dafounansou, A. Mohamadou, and T. C. Kofane, Modulational instability in nonlocal media with competing non-Kerr nonlinearities, Opt. Commun. **357**, 7 (2015).

[44] Y.-C. Zhang, V. Walther, and T. Pohl, Long-range interactions and symmetry breaking in quantum gases through optical feedback, Phys. Rev. Lett. **121**, 073604 (2018).

[45] F. Cinti, P. Jain, M. Boninsegni, A. Micheli, P. Zoller, and G. Pupillo, Supersolid droplet crystal in a dipole-blockaded gas, Phys. Rev. Lett. **105**, 135301 (2010).

[46] N. Henkel, F. Cinti, P. Jain, G. Pupillo, and T. Pohl, Supersolid vortex crystals in Rydberg-dressed Bose-Einstein condensates, Phys. Rev. Lett. **108**, 265301 (2012).

[47] C.-H. Hsueh, T.-C. Lin, T.-L. Horng, and W. C. Wu, Quantum crystals in a trapped Rydberg-dressed Bose-Einstein condensate, Phys. Rev. A **86**, 013619 (2012).

[48] Y.-C. Zhang, F. Maucher, and T. Pohl, Supersolidity around a critical point in dipolar Bose-Einstein condensates, Phys. Rev. Lett. **123**, 015301 (2019).

[49] Z. Shi and G. Huang, Selection and cloning of periodic optical patterns with a cold Rydberg atomic gas, Opt. Lett. **46**, 5344 (2021).

[50] Z. Shi, W. Li, and G. Huang, Structural phase transitions of optical patterns in atomic gases with microwave-controlled Rydberg interactions, Phys. Rev. A **102**, 023519 (2020).

[51] Z. Shi and G. Huang, Self-organized structures of two-component laser fields and their active controls in a cold Rydberg atomic gas, Phys. Rev. A **104**, 013511 (2021).

[52] Z. Bai and G. Huang, Enhanced third-order and fifth-order Kerr nonlinearities in a cold atomic system via Rydberg-Rydberg interaction, Opt. Express **24**, 4442 (2016).

[53] S. Mauger, J. Millen, and M. P. A. Jones, Spectroscopy of strontium Rydberg states using electromagnetically induced transparency, J. Phys. B **40**, F319 (2007).

[54] R. Mukherjee, J. Millen, R. Nath, M. P. A. Jones, and T. Pohl, Many-body physics with alkaline-earth Rydberg lattices, J. Phys. B **44**, 184010 (2011).

[55] C. L. Vaillant, M. P. A. Jones, and R. M. Potvliege, Long-range Rydberg-Rydberg interactions in calcium, strontium and ytterbium, J. Phys. B **45**, 135004 (2012).

[56] M. Wadati, Construction of parity-time symmetric potential through the soliton theory, J. Phys. Soc. Jpn. **77**, 074005 (2008).

[57] C. Hang and G. Huang, Parity-time symmetry along with nonlocal optical solitons and their active controls in a Rydberg atomic gas, Phys. Rev. A **98**, 043840 (2018).

[58] C. Hang, G. Huang, and V. V. Konotop, $\mathcal{PT}$-symmetry with a system of three-level atoms, Phys. Rev. Lett. **110**, 083604 (2013).

[59] T. B. Benjamin and J. E. Feir, The disintegration of wave trains on deep water, Theory, J. Fluid Mech. **27**, 417 (1967).

[60] D. A. Steck, Rubidium 87 D line data, http://steck.us/alkalidata.

[61] K. Singer, J. Stanojevic, M. Weidemuller, and R. Cote, Long-range interactions between alkali Rydberg atom pairs correlated to the *ns*-*ns*, *np*-*np* and *nd*-*nd* asymptotes, J. Phys. B **38**, S295 (2005).

[62] J. Yang, *Nonlinear Waves in Integrable and Non-Integrable Systems* (SIAM, Philadelphia, PA, 2010).

[63] H. Sakaguchi and B. A. Malomed, Dynamics of positive- and negative-mass solitons in optical lattices and inverted traps, J. Phys. B **37**, 1443 (2004).

[64] H. Sakaguchi and B. A. Malomed, Two-dimensional loosely and tightly bound solitons in optical lattices and inverted traps, J. Phys. B **37**, 2225 (2004).

[65] D. Christodoulides, F. Lederer, and Y. Silberberg, Discretizing light behaviour in linear and nonlinear waveguide lattices, Nature (London) **424**, 817 (2003).

[66] J. Yang and Z. H. Musslimani, Fundamental and vortex solitons in a two-dimensional optical lattice, Opt. Lett. **28**, 2094 (2003).